

# Graphene Contacts to a HfSe<sub>2</sub>/SnS<sub>2</sub> Heterostructure

Shanshan Su,\* Protik Das, and Roger K. Lake<sup>†</sup>

*Department of Electrical and Computer Engineering,  
University of California, Riverside, CA 92521, USA*

Supeng Ge

*Department of Physics and Astronomy,  
University of California, Riverside, CA 92521, USA*

(Dated: November 29, 2016)

## Abstract

Placing graphene on SnS<sub>2</sub> results in significant charge transfer, on the order of 10<sup>13</sup>/cm<sup>2</sup>, from the graphene to the SnS<sub>2</sub>, and the charge transfer results in a negative Schottky barrier contact for electron injection from the graphene into the SnS<sub>2</sub> conduction band. However, due to the  $s - p_{x,y}$  composition of the SnS<sub>2</sub> conduction band, the coupling between the SnS<sub>2</sub> and the graphene is relatively weak. A third layer, HfSe<sub>2</sub>, placed between the SnS<sub>2</sub> and the graphene, serves as a matrix element matching layer, since it has strong coupling to both the graphene and the SnS<sub>2</sub>. It increases the coupling to the graphene by a factor of 10, and it has little effect on the negative Schottky barrier height, since the conduction band wavefunction of the SnS<sub>2</sub> / HfSe<sub>2</sub> is a coherent superposition of the orbitals from the two individual layers, such that there is no energy barrier for an electron to move between the two layers. This paper first investigates the electronic properties of the heterostructure bilayer SnS<sub>2</sub> / HfSe<sub>2</sub> in the presence of an applied vertical electric field, and then it investigates the trilayer systems of BN / SnS<sub>2</sub> / HfSe<sub>2</sub> and graphene / SnS<sub>2</sub> / HfSe<sub>2</sub>. A tunneling Hamiltonian estimate of the the contact resistance of the graphene to the SnS<sub>2</sub> / HfSe<sub>2</sub> heterostructure indicates an excellent low-resistance contact.

## I. INTRODUCTION

Heterostructures of two-dimensional (2D) van der Waals (vdW) materials are being extensively investigated<sup>1-7</sup>. Recent studies of vdW heterostructures have shown that it is possible to build type II heterojunctions and nearly broken gap heterojunctions<sup>8-13</sup>. In type II heterojunctions, the electron-hole pair is separated both spatially and energetically enabling efficient photovoltaics and photodetection<sup>10,11</sup>. A few heterostructures composed of 2H transition metal dichalcogenides, such as  $\text{WSe}_2/\text{MoSe}_2$ , remain direct gap with the conduction and valence bands at  $K$ . The majority of heterostructures, such as, for example, black phosphorus/ $\text{MoS}_2$ <sup>8,9</sup> are indirect gap, with, in this particular case, the valence band at  $\Gamma$  and the conduction band at  $K$ . For electronic applications, multi-layer stacks of 2D materials such as black phosphorus/ $\text{SnSe}_2$ <sup>14</sup>,  $\text{WSe}_2/\text{SnSe}_2$ <sup>12,13</sup>, graphene/BN/graphene<sup>15</sup> and graphene/ $\text{WS}_2$ <sup>16</sup> are being exploited for tunnel devices and tunneling field-effect transistors (TFETs). There is also interest in using graphene to create direct bandgaps in multilayer heterostructures<sup>17-19</sup>, using graphene to make contact or tune other 2D materials<sup>20-28</sup>, and to tune the workfunction to enhance cold cathode emission<sup>29</sup>.

In the last application<sup>29</sup>, placing graphene on  $\text{SnS}_2$  significantly reduced the workfunction from that of  $\text{SnS}_2$  alone, and the charge transfer between the two materials resulted in p-type graphene and n-type  $\text{SnS}_2$ . The Fermi level of the composite aligned above the conduction band minimum of the  $\text{SnS}_2$ . From an electrical contact point of view, such an energetic alignment is a negative Schottky barrier contact, and it is highly desirable, since it gives a low contact resistance. But there are two barriers to inter-layer current flow. One barrier is the energetic barrier represented by the Schottky barrier height. In the graphene /  $\text{SnS}_2$  system, this barrier is negative, so it is very favorable. The other barrier is the inter-layer coupling between the two layers. This coupling depends on the matrix element between the Bloch functions of the bands in each layer that are being coupled. This matrix element will depend on the orbital composition of the bands and their positions in  $k$ -space<sup>30</sup>. We find that this coupling is weak between graphene and  $\text{SnS}_2$  near the Fermi level. To improve this coupling while maintaining a negative Schottky barrier, we investigate the use of a third material,  $\text{HfSe}_2$ , that serves as a ‘matrix element matching’ layer between the  $\text{SnS}_2$  and the graphene, since it has good coupling to both the  $\text{SnS}_2$  and the graphene.

In this paper, we analyze a multi-layer structure composed of monolayer  $\text{HfSe}_2$ ,  $\text{SnS}_2$ ,

graphene, and BN. Both  $\text{HfSe}_2$  and  $\text{SnS}_2$  are 1T polytype, hexagonal, 2D materials with indirect band gaps. In monolayer form, their conduction bands are at  $M$ , and their valence bands are at  $\Gamma$ . Stacking the two layers together creates an indirect-gap heterojunction that has type II qualities, but it does not fall cleanly into any one of the categories used to classify heterostructures of three-dimensional semiconductors, i.e. type I, type II, or type III, since the conduction bands strongly couple, and the wavefunction is distributed across both layers. An electric field applied to the heterostructure causes a shift in weight of the conduction band wavefunction from the  $\text{HfSe}_2$  layer to the  $\text{SnS}_2$  layer such that the band alignment takes on a type I quality. A commensurate stacking on graphene or BN using a  $2 \times 2$  supercell of the  $\text{HfSe}_2 / \text{SnS}_2$  and a  $3 \times 3$  supercell of the graphene or BN zone-folds the  $M$  point of the  $\text{HfSe}_2 / \text{SnS}_2$  back to  $\Gamma$ , and it zone-folds the  $K$  point of the graphene or BN back to  $\Gamma$  resulting in a direct-bandgap heterostructure. The strain between the two systems is low, 1.7% for the BN and 0.1% for the graphene. The charge transfer from the graphene to the  $\text{HfSe}_2 / \text{SnS}_2$  results in a negative Schottky barrier contact to the conduction band.

This paper is organized as follows. Sec. II describes the methods based on density functional theory. In Sec. III, AA and AB stacked heterostructures of  $\text{HfSe}_2 / \text{SnS}_2$  are first analyzed, and the effect of an applied vertical electric field is described. Then a third layer of either graphene or BN is added, and the tri-layer structures are analyzed and discussed. Conclusions are presented in Sec. IV.

## II. METHOD

Density functional theory calculations are performed with the Vienna *ab initio* simulation package (VASP)<sup>31–33</sup> in the projected-augmented-wave method<sup>34</sup>. The generalized gradient approximation (GGA) of the Perdew-Burke-Ernzerhof form<sup>35–37</sup> is used for the exchange correlation energy. The vdW interactions are included with the DFT-D2 method of Grimme<sup>38</sup>. The kinetic energy cutoff is 500 eV for all calculations. The first Brillouin zone is sampled with a  $8 \times 8 \times 1$   $\Gamma$ -centered Monkhorst-Pack grid. During all structural relaxations, the convergence tolerance on the Hellmann-Feynman forces is less than 0.01 eV $\text{\AA}$ . A vacuum layer larger than 25  $\text{\AA}$  is used for heterostructures to eliminate the interaction between adjacent images in the vertical direction. To determine more quantitative values for bandgaps, calculations are also performed with the hybrid Heyd-Scuseria-Ernzerhof (HSE) functional<sup>39</sup>.

The HSE calculations incorporate 25% short-range Hartree-Fock exchange. The screening parameter  $\mu$  is set to  $0.2 \text{ \AA}^{-1}$ .

The optimized lattice constant of  $\text{SnS}_2$  is  $3.69 \text{ \AA}$ , and the optimized lattice constant of  $\text{HfSe}_2$  is  $3.72 \text{ \AA}$ . The lattice mismatch between  $\text{SnS}_2$  and  $\text{HfSe}_2$  is less than 1%. The lattice constant of the heterostructure is set to the average value of  $3.70 \text{ \AA}$ . Monolayer  $\text{HfSe}_2$  and  $\text{SnS}_2$  are with bandgaps of  $1.1 \text{ eV}^{40}$  and  $2.4 \text{ eV}^{41}$ , respectively. As a check of the sensitivity of the electronic bandstructure to the lattice constant, we considered the two extreme cases resulting from exchanging the lattice constants of  $\text{HfSe}_2$  and  $\text{SnS}_2$ , and re-calculating the bandstructures of the individual layers. We found that the bandstructures of the individual material remained almost the same.

### III. RESULTS AND DISCUSSION

As shown in Fig. 1(a), we consider AA and AB stacking of  $\text{HfSe}_2$  on  $\text{SnS}_2$ . Both 1T bulk  $\text{HfSe}_2$  and  $\text{SnS}_2$  stack in AA order in which the metal atoms of one layer align with the metal atoms of the other. Sliding one layer with respect to the other such that the metal atoms of one layer align with the chalcogenide atoms of the other gives AB stacking. AA and AB stacking correspond to the two most stable stacking geometries. The total energy of the AA and AB stacked heterostructures are  $-6.053 \text{ eV}$  per atom and  $-6.050 \text{ eV}$  per atom, respectively. In  $k$ -space, both stacking arrangements have an indirect band gap with the conduction band minimum (CBM) at the  $M$  point and the valence band maximum (VBM) at  $\Gamma$ . In real-space, the CBM is more heavily weighted on the  $\text{SnS}_2$  layer, and the VBM is localized on the  $\text{HfSe}_2$  layer. The colors of the electronic bands in Fig. 1(c,d) indicate the layer on which the wavefunction is most heavily weighted as indicated in the legend. The PBE indirect bandgaps are  $237 \text{ meV}$  and  $224 \text{ meV}$  for the AA and AB structures, respectively. There are two conduction bands close to each other at the  $M$  point, and they originate from the conduction bands of the two individual layers. The energy gap between the two lowest conduction bands is  $316.5 \text{ meV}$  and  $285.3 \text{ meV}$  for AA and AB stacking, respectively.

A more quantitative determination of the energy spacings is made by calculating the electronic structure using the HSE hybrid functional. Qualitatively, the orbital composition and the order of the bands remain the same and the primary difference is that the conduction-

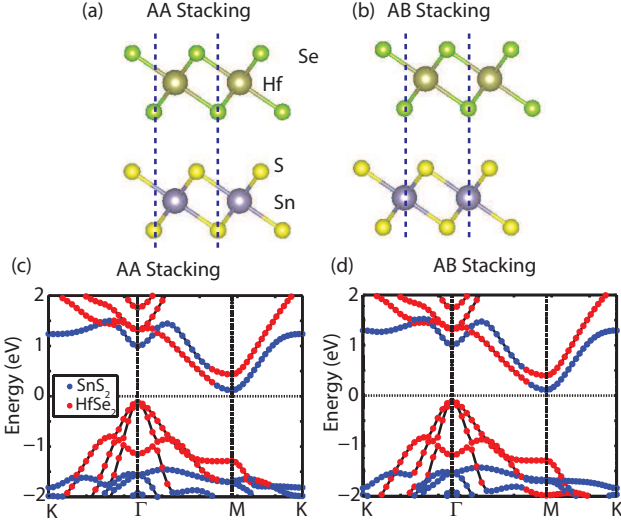


FIG. 1: Atomic structure of (a) AA stacking and (b) AB stacking. (c) AA electronic structure and (d) AB electronic structure.

valence bandgaps increase. The bandgaps increase to 0.88 eV and 0.89 eV for the AA and AB structures, respectively. However, the energy separation between the two conduction bands at  $M$  remains essentially unchanged with energies of 317.6 meV and 281.4 meV for AA and AB structures, respectively. This energy spacing between the two conduction bands is the critical energy that governs the crossing of the two conduction bands under an applied electric field. Since both the HSE and PBE calculations predict the same energy separation, we use the computationally less expensive PBE functional to predict the behavior of the heterostructure under applied cross-plane (vertical) electric fields. Furthermore, since the VBM remains strongly localized in the  $\text{HfSe}_2$  for all electric fields and multi-layer structures, the focus of the rest of the paper will be on the two lowest conduction bands and their evolution with electric field and in contact with graphene or BN.

When the two monolayers are brought together, the orbitals of the CBM in each layer will couple and push apart in energy. To understand the evolution of the bands as the two materials are brought together, we perform a DFT calculation of the AA structure with the two layers separated by 2 nm. This is sufficiently far apart that the bands do not interact, but a common Fermi level is enforced giving the band lineup of the well-separated, equilibrated, but non-interacting layers. The conduction band alignment of the separated system is shown in Fig. 2. When the layers are well-separated spatially, the energy separation of the two conduction bands is 0.25 eV. When the two layers are brought

together to form the heterostructure, the two conduction bands push further apart by 40 meV for AB stacking and 70 meV for AA stacking. This increase in energy separation is related to the coupling between the two bands, and the larger splitting in the AA structure indicates stronger coupling between the two conduction bands in that stacking arrangement.

For the spatially separated structure, the two conduction bands are 100% localized on the individual layers. The lower conduction band is localized on the  $\text{SnS}_2$ , and the upper conduction band is localized on the  $\text{HfSe}_2$ . In the  $\text{SnS}_2$ , the conduction band wavefunction is weighted 54% on the Sn, with 89% of that contribution from the s orbital, and 45% on the S, with 83% of that contribution from the  $p_x$  and  $p_y$  orbitals. In  $\text{HfSe}_2$ , the conduction band wavefunction is weighted 79% on the Hf. 96% of that comes from the d orbitals with the heaviest weight of 35% coming from  $d_{z^2}$ . The 21% contribution from Se is 61% from the  $p_z$  orbital, 22% from the d orbitals, and 9% from the s orbital.

When the two layers are brought together to form the AA heterostructure, the magnitude squared of the CBM wavefunction no longer remains localized on the  $\text{SnS}_2$ , but becomes distributed across both layers. It is weighted approximately 60% on the  $\text{SnS}_2$  and 40% on the  $\text{HfSe}_2$ . For the AB heterostructure, the wavefunction is weighted slightly more heavily on the  $\text{SnS}_2$ , with a weight of 67% on the  $\text{SnS}_2$  and 33% on the  $\text{HfSe}_2$ . The fact that the CBM wavefunction is weighted more heavily on the  $\text{SnS}_2$  layer is consistent with the weaker coupling inferred from the smaller splitting of the bands in the AB structure. The orbital compositions of the individual layers remain qualitatively the same as those of the isolated layers. The VBM always remains localized in the  $\text{HfSe}_2$  with an orbital composition from the  $p_x$  and  $p_y$  orbitals of the Se.

For both stacking arrangements, there is strong hybridization of the conduction band wavefunctions of the two individual layers, and the conventional spatially resolved band picture illustrated in Fig. 4(a) does not provide a good representation of the physics, at least for the conduction band. Instead, for the conduction band, the picture of bonding and anti-bonding molecular orbitals is more faithful to the underlying physics. In this picture the lower and upper conduction band at the M point are the bonding and anti-bonding combination of the isolated conduction bands of the individual layers. As the two layers are brought together, the bands couple and push apart resulting in two levels with the bonding orbital more heavily weighted on the  $\text{SnS}_2$ . However, there is no energy barrier for an electron to move between the two layers, since the CBM wavefunction is a coherent

superposition of the orbitals on both layers, and the probability of finding an electron on the  $\text{SnS}_2$  layer is at most a factor of 2 larger than on the  $\text{HfSe}_2$  layer.

By applying an electric field, the relative weights on each layer of the first conduction band can be altered and even reversed. As illustrated in Fig. 3(a), a positive electric field corresponds to a positive voltage applied to the  $\text{HfSe}_2$  layer, which means that the energy levels of the  $\text{HfSe}_2$  layer are lowered with respect to those in the  $\text{SnS}_2$  layer. Figs. 3(b) and (c) show the AA electronic structure under forward and reverse bias, respectively. Under forward bias, the spectral weight of the CBM switches from the  $\text{SnS}_2$  to the  $\text{HfSe}_2$ .

The orbital compositions of the CBMs are illustrated in Figs. 4 for three different electric fields,  $-0.4 \text{ V}/\text{\AA}$ ,  $0 \text{ V}/\text{\AA}$ , and  $0.4 \text{ V}/\text{\AA}$ , corresponding to the left, middle, and right columns, respectively. Fig. 4(a) illustrates the band alignments with the usual band picture used for bulk semiconductor heterojunctions for the 3 different electric fields. The left side of each band diagram represents the  $\text{HfSe}_2$  layer and the right side represents the  $\text{SnS}_2$  layer. The energy level of the CBM only indicates on which layer it is more heavily weighted.

As the electric field is ramped from negative to positive, the spectral weight gradually shifts from the  $\text{SnS}_2$  to the  $\text{HfSe}_2$ . This shift of the wavefunction is illustrated in Fig. 5 for the AA and AB heterostructures. Fig. 5 shows the energies of the two lowest CBMs with the energy reference taken as the middle of the PBE bandgap. The percentages give the percent spectral weight of the wavefunction on the layer indicated by the label adjacent to each line. The trends and quantitative values for the AA and the AB stacked heterostructures are very

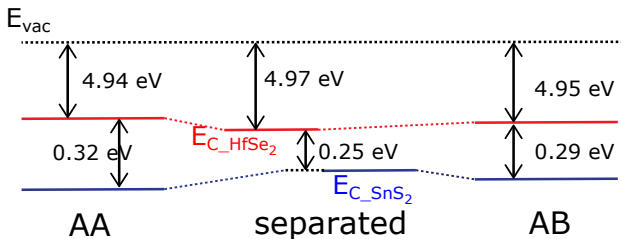


FIG. 2: The two lowest conduction band edges of the spatially separated  $\text{HfSe}_2/\text{SnS}_2$  system (center), the AA stacked heterostructure (left), and AB stacked heterostructure (right).  $E_{\text{vac}}$  is the energy level of vacuum. In the well-separated case, the blue line is the conduction band edge of  $\text{SnS}_2$ , and the red line is the conduction band edge of  $\text{HfSe}_2$ . For the AA and AB heterostructures, the red and blue lines indicate on which layer the conduction band edge wavefunction is most heavily weighted.

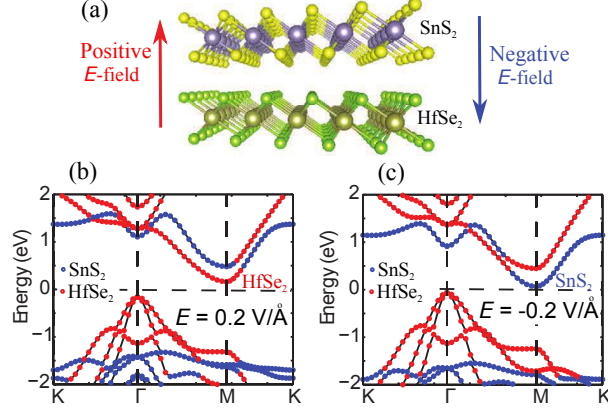


FIG. 3: (a) The AA heterostructure with arrows showing the direction of the applied electric fields ( $\mathcal{E}$ ) for the energy wavevector plots underneath. (b) Bandstructure of the AA heterostructure under forward bias ( $\mathcal{E} = 0.2 \text{ V/}\text{\AA}$ ). The HfSe<sub>2</sub> and SnS<sub>2</sub> CBMs have switched. (c) Bandstructure of the AA heterostructure under reverse bias ( $\mathcal{E} = -0.2 \text{ V/}\text{\AA}$ ).

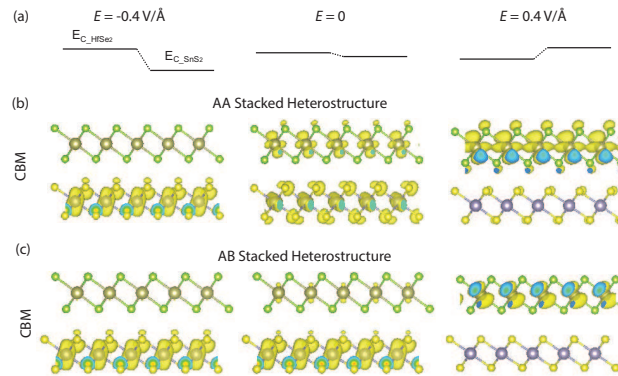


FIG. 4: (a) Schematic view of band alignments under  $-0.4 \text{ V/}\text{\AA}$ ,  $0 \text{ V/}\text{\AA}$ , and  $0.4 \text{ V/}\text{\AA}$ . (b) Isosurfaces of the orbital resolved wave-functions of the CBM of the AA stacked heterostructure under applied electric fields of  $-0.4$ ,  $0$ , and  $0.4 \text{ V/}\text{\AA}$ . (c) Isosurfaces of band resolved wave-functions of the CBM and of the AB stacked heterostructure under applied electric fields of  $-0.4$ ,  $0$ , and  $0.4 \text{ V/}\text{\AA}$ .

similar. At zero field, the CBM is weighted towards the SnS<sub>2</sub> as previously discussed. At negative fields, the CBM wavefunction becomes more localized on the SnS<sub>2</sub> layer. A shift in the CBM weight from the SnS<sub>2</sub> to the HfSe<sub>2</sub> layer occurs between positive fields of  $0.1$  and  $0.2 \text{ V/}\text{\AA}$ . As the field becomes more positive the CBM wavefunction becomes more localized on the HfSe<sub>2</sub>.

Two dimensional materials will be in contact with other materials as contacts, substrate,

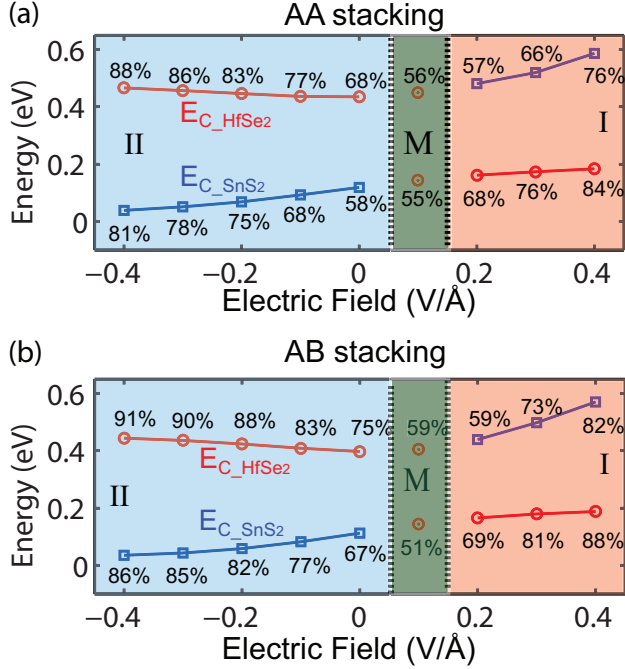


FIG. 5: (a) Evolution of the two lowest conduction band edges as a function of electric field for the (a) AA and (b) AB heterostructures.  $E_{C_{\text{HfSe}_2}}$  is the CBM of  $\text{HfSe}_2$ , and  $E_{C_{\text{SnS}_2}}$  is the CBM of  $\text{SnS}_2$ . The weights of  $\text{HfSe}_2$  and  $\text{SnS}_2$  are marked on  $E_{C_{\text{HfSe}_2}}$  and  $E_{C_{\text{SnS}_2}}$ , respectively. Region II and region I correspond to heterojunction type II and type I respectively. Region M represents the region that the two lowest conduction bands with heavily mixed contributions from the two layers of materials.

or encapsulation to prevent oxidation. All-2D systems are very attractive since the interfaces are self-passivated and devoid of dangling bonds. BN is a good insulator, and has recently been demonstrated to protect highly reactive black phosphorous from oxidation<sup>42</sup>. Graphene, a good conductor, is closely lattice matched to BN. A  $3 \times 3$  supercell of graphene or BN is also very closely lattice matched to a  $2 \times 2$  supercell of  $\text{HfSe}_2/\text{SnS}_2$ . The lattice constants of BN and graphene are  $2.51 \text{ \AA}$ , and  $2.47 \text{ \AA}$ , respectively. The lattice mismatches between the BN or graphene  $3 \times 3$  supercells and the  $\text{HfSe}_2/\text{SnS}_2$   $2 \times 2$  supercell are 1.7% and 0.1%, respectively. The lattice constant of the supercell is fixed to be the lattice constant of the  $\text{HfSe}_2/\text{SnS}_2$  heterostructure, so that the the  $\text{HfSe}_2/\text{SnS}_2$  heterostructure remains unstrained.

The tri-layer systems are stable. The formation energies are negative, and they are listed below in units of eV per primitive unit cell (UC) of the BN or graphene, where one primitive

unit cell consists of two atoms. For BN on  $\text{HfSe}_2/\text{SnS}_2$  as shown in Fig. 6, the formation energy is  $-0.087 \text{ eV/UC}$ . The formation energies for graphene on the  $\text{HfSe}_2$  side or the  $\text{SnS}_2$  side of the AA stacked heterostructure shown in Fig. 7 are  $-0.232 \text{ eV/UC}$  or  $-0.185 \text{ eV/UC}$ , respectively. The formation energies for graphene on the  $\text{HfSe}_2$  side or the  $\text{SnS}_2$  side of the AB stacked heterostructure are very similar, and they are  $-0.240 \text{ eV/UC}$  and  $-0.193 \text{ eV/UC}$ , respectively. Therefore, the trilayer systems are stable, and the graphene tri-layer structures are most stable.

Fig. 6(a) shows the structure and supercell of a BN monolayer on the  $\text{HfSe}_2$  layer of the  $\text{HfSe}_2/\text{SnS}_2$  heterostructure. The electronic bandstructures for the AA and AB heterostructures with BN on the  $\text{HfSe}_2$  layer are shown in Figs. 6(b) and (c), respectively. The bands of the  $\text{HfSe}_2/\text{SnS}_2$  layers show no noticeable change due to the proximity of the BN. The BN bands are far from the Fermi energy and are buried deep in the valence and conduction bands of the  $\text{HfSe}_2/\text{SnS}_2$  as one would expect for a wide bandgap insulator. Only the BN valence band can be seen on this energy scale. What is most notable about this energy-momentum plot is that all of the band edges now occur at  $\Gamma$ . This is a result of zone-folding. The  $2 \times 2$  supercell of the  $\text{HfSe}_2/\text{SnS}_2$  folds the  $M$  points back to  $\Gamma$ , and the  $3 \times 3$  supercell of the BN folds the  $K$  points back to  $\Gamma$ . Thus, the system becomes direct gap. The zone-folding of the different Brillouin zones is illustrated in Fig. 6(a).

Placing graphene on either the  $\text{HfSe}_2$  layer or the  $\text{SnS}_2$  layer of the AA or AB stacked heterostructures results in charge transfer from the graphene to the  $\text{HfSe}_2/\text{SnS}_2$  heterostructure such that the graphene becomes p-type, the  $\text{HfSe}_2/\text{SnS}_2$  becomes n-type, and the Fermi level aligns above the CBM of the  $\text{HfSe}_2/\text{SnS}_2$ . The structures and energy-momentum relations are shown in Figs. 7(a-d) and 8(a-d) for graphene on the top or bottom of the AA or AB heterostructures, respectively. The charge transfer  $n_s$  can be estimated by position of the Dirac point of the graphene  $E_D$  with respect to the Fermi level  $E_F$  as  $n_s = \frac{1}{\pi(\hbar v)^2} (E_D - E_F)^2$ . With graphene on  $\text{HfSe}_2$ ,  $E_D - E_F = 0.335 \text{ eV}$ , and  $n_s = 1.26 \times 10^{13} \text{ cm}^{-2}$ . With graphene on  $\text{SnS}_2$ ,  $E_D - E_F = 0.430 \text{ eV}$ , and  $n_s = 2.07 \times 10^{13} \text{ cm}^{-2}$ . The calculated results are very close to the Bader charge transfer<sup>43</sup> results,  $1.13 \times 10^{13} \text{ cm}^{-2}$  with graphene on  $\text{HfSe}_2$  and  $1.33 \times 10^{13} \text{ cm}^{-2}$  with graphene on  $\text{SnS}_2$ , obtained from VASP. By electronic device standards, this sheet charge density transferred from the graphene into the  $\text{HfSe}_2/\text{SnS}_2$  is large. The electron transfer from the graphene to the  $\text{HfSe}_2/\text{SnS}_2$  is accompanied by a lowering of the potential of the layer in contact with the graphene. The region of the electronic bands

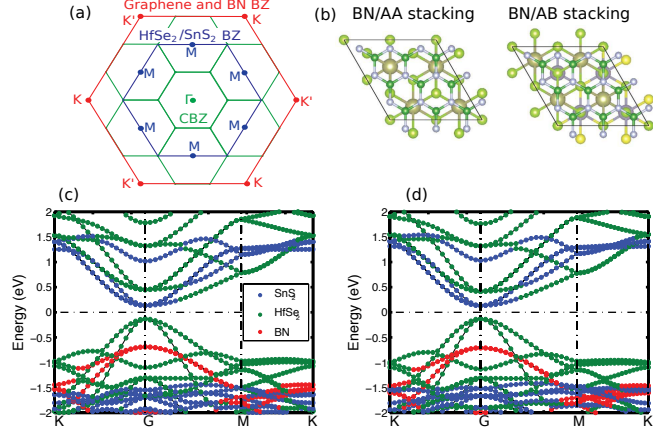


FIG. 6: BN on HfSe<sub>2</sub>/SnS<sub>2</sub>. (a) Brillouin zone folding resulting from the  $2 \times 2$  unit cell of the HfSe<sub>2</sub>/SnS<sub>2</sub> and the  $3 \times 3$  unit cell of the BN or graphene. The outer Brillouin zone (BZ) in red is the BZ of the graphene or BN. The BZ in blue is the BZ of the HfSe<sub>2</sub>/SnS<sub>2</sub>. The innermost BZ in green is the commensurate BZ (CBZ) of the supercell. The CBZ is tiled over the entire  $k$ -space region to show that the  $M$  point of the blue BZ lies at the  $\Gamma$  point of the first repeated CBZ, and the  $K$  point of the red BZ lies at the  $\Gamma$  point of the second repeated CBZ. (b) Atomistic structures for BN on AA and AB stacked HfSe<sub>2</sub>/SnS<sub>2</sub>. (c) Electronic bandstructure for AA stacking. (d) Electronic bandstructure for AB stacking. In (c) and (d), the color indicates on which layer the wavefunction is most heavily weighted.

around the Fermi level near  $\Gamma$  is shown in Figs. 7(e-f) and 8(e-f). In all cases, the lowest conduction band wavefunction is weighted more heavily towards the layer in contact with the graphene. This results in a negative Schottky barrier between the graphene and the conduction band of HfSe<sub>2</sub>/SnS<sub>2</sub> for contact to either side of the heterostructure.

For a good contact, energy level alignment is critical, but there should also be coupling between the graphene and the HfSe<sub>2</sub>/SnS<sub>2</sub> layers for electrons to transfer easily between the two layers. This coupling or interaction appears in the energy-momentum plots as an anti-crossing of the graphene and HfSe<sub>2</sub>/SnS<sub>2</sub> bands. The anti-crossing of the graphene band and the HfSe<sub>2</sub>/SnS<sub>2</sub> conduction band is shown in Figs. 7(e,f) and 8(e,f). The color coding of the bands is the same as in Figs. 7(c,d) and 8(c,d). In this commensurate Brillouin zone, the conduction band of the HfSe<sub>2</sub>/SnS<sub>2</sub> is 3-fold degenerate (excluding spin), since the 6  $M$  points of the original HfSe<sub>2</sub>/SnS<sub>2</sub> Brillouin zone are folded to  $\Gamma$ . The Dirac cone of the graphene is two-fold degenerate, since the  $K$  and  $K'$  points of the original graphene

Brillouin zone are folded to  $\Gamma$ . Where the bands anti-cross shown in the region of the vertical ellipses, the interaction between the graphene and the  $\text{HfSe}_2$  breaks the degeneracy, so that the 2 Dirac cones and 3 conduction bands from the  $\text{HfSe}_2/\text{SnS}_2$  can be clearly seen in Figs. 7(e) and 8(e). In Figs. 7(e) and 8(e), the Dirac cone of the graphene anti-crosses with the conduction bands of the  $\text{HfSe}_2/\text{SnS}_2$  with an energy splitting  $\Delta$  on the order of 100 meV. A value for the coupling  $t$  can be estimated from the energy splitting  $\Delta$  of the splitting of bands at the crossing points. Setting  $\Delta = 2t$ , gives  $t \approx 50$  meV. In the energy-momentum region where the bands anti-cross indicated by the vertical ellipses, the wavefunction composition is a mix of orbitals from the graphene and the  $\text{HfSe}_2/\text{SnS}_2$ . The composition of the three bands circled by the left ellipse in Fig. 7(e) are, from lowest energy to highest energy: (1) 26%  $\text{SnS}_2$ , 44%  $\text{HfSe}_2$ , and 29% of graphene; (2) 22%  $\text{SnS}_2$ , 38%  $\text{HfSe}_2$ , and 40% graphene; and (3) 48%  $\text{SnS}_2$ , 47%  $\text{HfSe}_2$ , and 4% graphene. The orbital composition of the bands circled by the right ellipse along the line from  $\Gamma$  to  $M$  are very similar. Thus, both the energetic splitting and the orbital mixing indicate that there is significant coupling between the graphene and the  $\text{HfSe}_2$  layer that should allow easy charge transfer between the layers under applied bias.

The interaction of graphene with  $\text{HfSe}_2$  is larger than with  $\text{SnS}_2$ , and this is consistent with the orbital composition of the conduction bands of  $\text{HfSe}_2$  and  $\text{SnS}_2$ . The conduction band of  $\text{HfSe}_2$  has large Hf  $d_{z^2}$  and Se  $p_z$  components that would be expected to couple well to the C  $p_z$  orbitals of the graphene. The conduction band of  $\text{SnS}_2$  has large Sn  $s$  and S  $p_x, p_y$  components. The in-plane S  $p_x, p_y$  orbitals would be expected to couple poorly to the C  $p_z$  orbitals of the graphene. When the graphene is placed on the  $\text{SnS}_2$  layer, the bands near the Fermi level shown in Fig. 7(f) look qualitatively different compared to the bands with graphene on the  $\text{HfSe}_2$  layer. At  $\Gamma$ , the 3 conduction bands of the  $\text{HfSe}_2/\text{SnS}_2$  remain degenerate. All 3 of the conduction bands now lie 0.03 eV below the Fermi level, so that the Schottky barrier becomes more negative. This is consistent with the fact that, as shown in Fig. 2, the conduction band of the  $\text{SnS}_2$  is energetically lower than that of  $\text{HfSe}_2$ , and the conduction band wavefunction of the isolated  $\text{HfSe}_2/\text{SnS}_2$  heterostructure is more heavily weighted towards the  $\text{SnS}_2$  layer as shown in Fig. 1. The energy alignment is more favorable for electrical contact, however the coupling between the graphene and the  $\text{SnS}_2$  is considerably weaker. Now, the maximum energy splitting is  $\approx 10$  meV giving an estimate for the coupling of  $t \approx 5$  meV.

The difference in coupling can also be seen in the composition of the conduction band wavefunctions at the  $\Gamma$  point. For graphene on  $\text{HfSe}_2$ , at the  $\Gamma$  point, the compositions of the three conduction bands nearest the Fermi energy, from lowest to highest energy are: (1) 40%  $\text{SnS}_2$ , 54%  $\text{HfSe}_2$ , and 5% graphene; (2) 40%  $\text{SnS}_2$ , 55%  $\text{HfSe}_2$ , and 5% of graphene; and (3) 48% of  $\text{SnS}_2$ , 52% of  $\text{HfSe}_2$ , and 0% graphene. The highest split-off conduction band has its weight shifted more towards the  $\text{SnS}_2$  layer compared to the lower two conduction bands, and it has no graphene contribution. With graphene on the  $\text{SnS}_2$ , the compositions of the three conduction bands nearest the Fermi energy at the  $\Gamma$  point, are all the same, and they are 65%  $\text{SnS}_2$ , 35%  $\text{HfSe}_2$ , and 0% graphene.

The trends for graphene on the AB stacked structure are qualitatively the same as for graphene on the AA structure. As discussed with respect to Fig. 2, the interlayer coupling between the  $\text{SnS}_2$  and  $\text{HfSe}_2$  is weaker in the AB stacking arrangement compared to that with AA stacking. Therefore, the wavefunction of the conduction band edge is more heavily weighted towards the  $\text{SnS}_2$  in the isolated heterostructure. In the AB structure, placing the graphene on the  $\text{HfSe}_2$ , reverses the weight of the bottom two conduction bands in Fig. 8, so that their compositions become (1) 43%  $\text{SnS}_2$ , 51%  $\text{HfSe}_2$ , and 5% graphene; and (2) 43%  $\text{SnS}_2$ , 52%  $\text{HfSe}_2$ , and 5% graphene. The spectral weight of the highest band is 52%  $\text{SnS}_2$ , 48%  $\text{HfSe}_2$ , and 0% graphene. The only qualitative difference between this structure and the AA structure is the slight shift in orbital weight of the conduction band wavefunction towards the  $\text{SnS}_2$ .

The values of the interlayer couplings  $t$  can be used in a tunneling Hamiltonian expression to estimate the interlayer conductance between the graphene and the  $\text{HfSe}_2/\text{SnS}_2$  heterostructure when graphene is placed on either the  $\text{SnS}_2$  layer or the  $\text{HfSe}_2$  layer. The interlayer conductivity can be written as,

$$\sigma_c = \frac{g_s g_G g_H e^2}{\mathcal{A} h} \sum_{\mathbf{k}} \int dE A_G(\mathbf{k}; E) A_H(\mathbf{k}; E) |t|^2 \frac{-\partial f(E - E_f)}{\partial E}, \quad (1)$$

where  $A_G(\mathbf{k}; E)$  and  $A_H(\mathbf{k}; E)$  are spectral functions of the graphene layer and the semiconductor heterostructure, respectively,  $g_s = 2$  is the spin degeneracy,  $g_G = 2$  is the graphene band degeneracy,  $g_H = 3$  is the  $\text{HfSe}_2/\text{SnS}_2$  band degeneracy,  $\mathcal{A}$  is the cross-sectional area,  $f(E - E_f)$  is the Fermi-Dirac factor,  $E_f$  is the Fermi level, and  $t$  is the interlayer coupling. The spectral functions are  $A_G(\mathbf{k}; E) = \frac{\gamma}{(E + \hbar v_F k - \varepsilon_D)^2 + \gamma^2/4}$ ,  $A_H(\mathbf{k}; E) = \frac{\gamma}{(E - \frac{\hbar^2 k^2}{2m^*} - \varepsilon_H)^2 + \gamma^2/4}$ , where  $\gamma$  is the lifetime broadening,  $m^* = 0.4m_0$  is the effective mass obtained from the DFT

bandstructures in Fig. 7(c)-(d),  $v_F = 0.81 \times 10^6$  m/s is the Fermi velocity of graphene,  $\varepsilon_D$  is the energy of the Dirac point, and  $\varepsilon_H$  is the energy of the conduction band minimum of the HfSe<sub>2</sub>/SnS<sub>2</sub> heterostructure. For a given transverse  $\mathbf{k}$ , the quantity  $T(E, \mathbf{k}) = A_G(\mathbf{k}; E)A_H(\mathbf{k}; E)|t|^2$  is the transmission coefficient, and, as such, its value must lie between 0 and 1.<sup>30</sup> The values of  $\varepsilon_D$  and  $\varepsilon_H$  are chosen such that the lower Dirac cone of the graphene and the parabolic conduction band of the HfSe<sub>2</sub>/SnS<sub>2</sub> intersect at the Fermi wavevector  $k_F$ ,  $(E_F + \hbar v_F k_F - \varepsilon_D) = (E_F - \frac{\hbar^2 k_F^2}{2m^*} - \varepsilon_H) = 0$ , giving a maximum value for  $T(E, \mathbf{k})$  of  $16|t|^2/\gamma^2 \leq 1$ . This, sets a lower limit on the value for  $\gamma$  of  $\gamma \geq 4|t|$ . For graphene on HfSe<sub>2</sub>,  $t$  is large,  $\approx 50$  meV, which pushes the limit of validity of the tunneling Hamiltonian expression (1), and it requires a large value for  $\gamma$  of 200 meV. The contact resistance is  $R_C = 1/\sigma_c$ , and the resulting value for the contact resistance of graphene on HfSe<sub>2</sub> as shown in Fig. 7(a) is  $1 \text{ m}\Omega \cdot \mu\text{m}^2$ . With graphene on SnS<sub>2</sub>,  $t \approx 5$  meV, and the contact resistance is  $100 \text{ m}\Omega \cdot \mu\text{m}^2$ . The resistances scale as  $|t|^2$ , which accounts for the factor of 100 difference in the contact resistances. Decreasing the value of  $\gamma$  monotonically decreases  $R_C$  by approximately a factor of 5 as  $\gamma$  is decreased from 200 meV to 20 meV. These resistance values should be viewed as order-of-magnitude estimates. Both of these values are excellent in terms of the state-of-the art contact resistance to 2D materials<sup>44</sup>, and the lowest value is competitive with the best that has been achieved in the well-developed semiconductors such as InGaAs<sup>45</sup>.

#### IV. SUMMARY AND CONCLUSIONS

Monolayer HfSe<sub>2</sub> and SnS<sub>2</sub> are closely lattice matched with a strain of less than 1%, an average lattice constant of 3.70 Å, and bandgaps of 1.1 eV<sup>40</sup> and 2.4 eV<sup>41</sup>, respectively. When the two materials are well-separated, but with a common Fermi level, the HfSe<sub>2</sub> conduction band is 0.25 eV above the SnS<sub>2</sub> conduction band, and the valence band of the HfSe<sub>2</sub> is more than 1 eV above the valence band of the SnS<sub>2</sub>. Such a band lineup in traditional three dimensional semiconductors leads to a type II heterostructure in which the conduction band is on one layer and the valence band is on the other. However, when the HfSe<sub>2</sub> and the SnS<sub>2</sub> are brought together to form a heterostructure, the conduction band minimum at  $M$  becomes a coherent superposition of the conduction band wavefunctions of the individual layers. The conduction band wavefunction is weighted 60% on the SnS<sub>2</sub> and

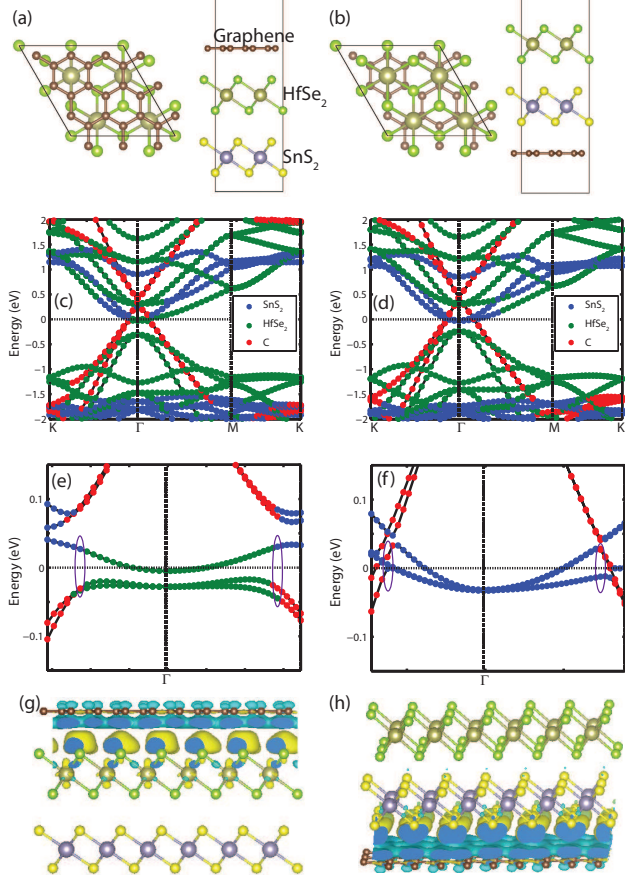


FIG. 7: Trilayer of graphene and AA stacked HfSe<sub>2</sub>/SnS<sub>2</sub>. (a) Atomic structure of graphene on the HfSe<sub>2</sub> layer. (b) Atomic structure of graphene on the SnS<sub>2</sub> layer. (c) and (e) are the corresponding electronic structure plots. (e) focuses on the small energy range near the Fermi level. (g) shows the charge transfer at the interface. (d) and (f) are the corresponding electronic structure plots. (f) focuses on the small energy range near the Fermi level. (h) shows the charge transfer at the interface. In (g) and (h), the charge accumulation and depletion is denoted by the yellow and blue color, respectively. The Fermi level is at  $E = 0$ . The purple circles in (e) and (f) indicate the anti-crossing of the graphene hole band and the HfSe<sub>2</sub>/SnS<sub>2</sub> conduction band.

40% on the HfSe<sub>2</sub> for AA stacking and 67% on the SnS<sub>2</sub> and 33% on the HfSe<sub>2</sub> for AB stacking. There is no energy barrier for an electron to move between the two layers, since the conduction band wavefunction is a coherent superposition of the orbitals of both layers. A vertical electric field of 0.2 V/Å pointing from the HfSe<sub>2</sub> layer to the SnS<sub>2</sub> layer reverses the weights of the conduction band wavefunction to approximately 70% HfSe<sub>2</sub> and 30% SnS<sub>2</sub>. In the SnS<sub>2</sub>, the primary orbital contributions come from the *s*-orbital of the Sn and

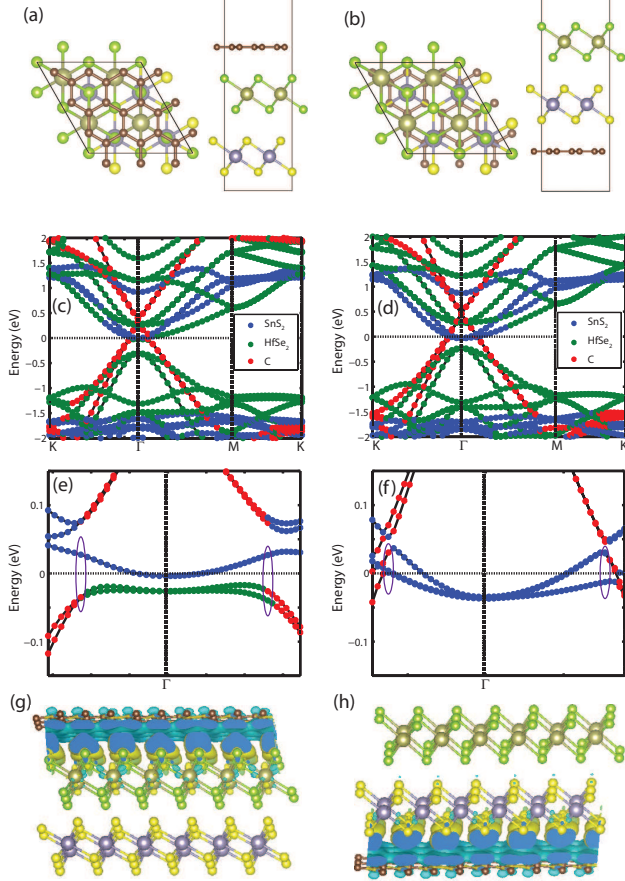


FIG. 8: Trilayer of graphene and AB stacked HfSe<sub>2</sub>/SnS<sub>2</sub>. (a) Atomic structure of graphene on the HfSe<sub>2</sub> layer. (b) Atomic structure of graphene on the SnS<sub>2</sub> layer. (c) and (e) are the corresponding electronic structure plots. (e) focuses on the small energy range near the Fermi level. (g) shows the charge transfer at the interface. (b) and (d) are the corresponding electronic structure plots. (f) focuses on the small energy range near the Fermi level. (h) shows the charge transfer at the interface. In (g) and (h), the charge accumulation and depletion is denoted by the yellow and blue color, respectively. The Fermi level is at  $E = 0$ . The purple circles in (e) and (f) indicate the anti-crossing of the graphene hole band and the HfSe<sub>2</sub>/SnS<sub>2</sub> conduction band.

the  $p_{x,y}$  orbitals of the S. In the HfSe<sub>2</sub>, the primary orbital contributions come from the  $d_{z^2}$  orbital of the Hf and the  $p_z$  orbital of the Se. The valence band maximum at  $\Gamma$  is localized on the HfSe<sub>2</sub> layer, and its dominant orbital contributions come from the  $p_x$  and  $p_y$  orbitals of the Se. The calculated HSE bandgap of the AA and AB heterostructures are 0.88 eV and 0.89 eV, respectively.

A  $3 \times 3$  supercell of graphene is almost perfectly lattice matched to a  $2 \times 2$  supercell

of  $\text{HfSe}_2/\text{SnS}_2$  with a lattice mismatch of 0.1%. The trilayer heterostructure is stable with negative formation energies, and the formation energy with graphene on the  $\text{HfSe}_2$  is approximately 50 meV more negative than with graphene on the  $\text{SnS}_2$ . This indicates a stronger interaction of the graphene with the  $\text{HfSe}_2$ , which is consistent with the results from the electronic structure calculations. A charge density on the order of  $10^{13}/\text{cm}^2$  transfers from the graphene to the  $\text{HfSe}_2/\text{SnS}_2$  resulting in a Fermi level that aligns within the conduction band of the the  $\text{HfSe}_2/\text{SnS}_2$  and a negative Schottky barrier contact for electron injection into the conduction band. The coupling of the graphene to the  $\text{HfSe}_2$  is approximately 10 times larger than the coupling of the graphene to the  $\text{SnS}_2$ , and this is consistent with the  $d_{z^2}$  and  $p_z$  orbital composition of the  $\text{HfSe}_2$  conduction band compared to the  $s$  and  $p_{x,y}$  composition of the  $\text{SnS}_2$  conduction band. A tunneling Hamiltonian estimate for the contact resistance of graphene on the  $\text{HfSe}_2$  layer versus graphene on the  $\text{SnS}_2$  layer gives contact resistances of  $1 \text{ m}\Omega\mu\text{m}^2$  and  $100 \text{ m}\Omega\mu\text{m}^2$ , respectively. Both values would be considered exceptional for 2D materials, and the lowest value is competitive with lowest contact resistances measured in 3D semiconductors such as InGaAs.

*Acknowledgements:* This work is supported in part by FAME, one of six centers of STARnet, a Semiconductor Research Corporation program sponsored by MARCO and DARPA, and by the NSF EFRI-143395. This work used the Extreme Science and Engineering Discovery Environment (XSEDE), which is supported by National Science Foundation grant number ACI-1053575.

---

\* ssu008@ucr.edu

† rlake@ece.ucr.edu

<sup>1</sup> Cheng Gong, Hengji Zhang, Weihua Wang, Luigi Colombo, Robert M. Wallace, and Kyeongjae Cho, “Band alignment of two-dimensional transition metal dichalcogenides: Application in tunnel field effect transistors,” *Applied Physics Letters* **103**, 053513 (2013).

<sup>2</sup> Jun Kang, Sefaattin Tongay, Jian Zhou, Jingbo Li, and Junqiao Wu, “Band offsets and heterostructures of two-dimensional semiconductors,” *Applied Physics Letters* **102**, 012111 (2013).

<sup>3</sup> Lei Fu, Yangyong Sun, Nian Wu, Rafael G. Mendes, Linfeng Chen, Zhen Xu, Tao Zhang,

Mark H. Rmmeli, Bernd Rellinghaus, Darius Pohl, Lin Zhuang, and Lei Fu, "Direct growth of MoS<sub>2</sub>/h-BN heterostructures via a sulfide-resistant alloy," *ACS Nano* **10**, 2063–2070 (2016).

<sup>4</sup> Gwan-Hyoung Lee, Young-Jun Yu, Xu Cui, Nicholas Petrone, Chul-Ho Lee, Min Sup Choi, Dae-Yeong Lee, Changgu Lee, Won Jong Yoo, Kenji Watanabe, Takashi Taniguchi, Colin Nuckolls, Philip Kim, and James Hone, "Flexible and transparent mos<sub>2</sub> field-effect transistors on hexagonal boron nitride-graphene heterostructures," *ACS nano* **7**, 7931–7936 (2013).

<sup>5</sup> Chul-Ho Lee, Gwan-Hyoung Lee, Arend M. van der Zande, Wenchao Chen, Yilei Li, Minyong Han, Xu Cui, Ghidewon Arefe, Colin Nuckolls, Tony F. Heinz, Jing Guo, James Hone, and Philip Kim, "Atomically thin pn junctions with van der waals heterointerfaces," *Nat Nano* **9**, 676–681 (2014).

<sup>6</sup> Radhakrishnan Balu, Xiaoliang Zhong, Ravindra Pandey, and Shashi P. Karna, "Effect of electric field on the band structure of graphene/boron nitride and boron nitride/boron nitride bilayers," *Applied Physics Letters* **100**, 052104 (2012).

<sup>7</sup> Jie Su, Li-ping Feng, Hai-xi Pan, Hong-cheng Lu, and Zheng-tang Liu, "Modulating the electronic properties of monolayer MoS<sub>2</sub> through heterostructure with monolayer gray arsenic," *Materials & Design* **96**, 257–262 (2016).

<sup>8</sup> Le Huang, Yan Li, Zhongming Wei, and Jingbo Li, "Strain induced piezoelectric effect in black phosphorus and MoS<sub>2</sub> van der waals heterostructure," *Scientific Reports* **5**, 16448 (2015).

<sup>9</sup> Le Huang, Nengjie Huo, Yan Li, Hui Chen, Juehan Yang, Zhongming Wei, Jingbo Li, and Shu-Shen Li, "Electric-field tunable band offsets in black phosphorus and MoS<sub>2</sub> van der waals p-n heterostructure," *J. Phys. Chem. Lett.* **6**, 2483–2488 (2015).

<sup>10</sup> Krzysztof Kośmider and Joaquín Fernández-Rossier, "Electronic properties of the MoS<sub>2</sub>-WS<sub>2</sub> heterojunction," *Phys. Rev. B* **87**, 075451 (2013).

<sup>11</sup> Marco Bernardi, Maurizia Palummo, and Jeffrey C Grossman, "Extraordinary sunlight absorption and one nanometer thick photovoltaics using two-dimensional monolayer materials," *Nano letters* **13**, 3664–3670 (2013).

<sup>12</sup> M. O. Li, D. Esseni, J. J. Nahas, D. Jena, and H. G. Xing, "Two-dimensional heterojunction interlayer tunneling field effect transistors (thin-TFETs)," *IEEE Journal of the Electron Devices Society* **3**, 200–207 (2015).

<sup>13</sup> R Schlaf, O Lang, C Pettenkofer, and W Jaegermann, "Band lineup of layered semiconductor heterointerfaces prepared by van der waals epitaxy: Charge transfer correction term for the

electron affinity rule,” *Journal of applied physics* **85**, 2732–2753 (1999).

<sup>14</sup> Rusen Yan, Sara Fathipour, Yimo Han, Bo Song, Shudong Xiao, Mingda Li, Nan Ma, Vladimir Protasenko, David A Muller, Debdeep Jena, *et al.*, “Esaki diodes in van der waals heterojunctions with broken-gap energy band alignment,” *Nano letters* **15**, 5791–5798 (2015).

<sup>15</sup> L Britnell, RV Gorbachev, R Jalil, BD Belle, F Schedin, A Mishchenko, T Georgiou, MI Katsnelson, L Eaves, SV Morozov, *et al.*, “Field-effect tunneling transistor based on vertical graphene heterostructures,” *Science* **335**, 947–950 (2012).

<sup>16</sup> Thanasis Georgiou, Rashid Jalil, Branson D Belle, Liam Britnell, Roman V Gorbachev, Sergey V Morozov, Yong-Jin Kim, Ali Gholinia, Sarah J Haigh, Oleg Makarovsky, *et al.*, “Vertical field-effect transistor based on graphene-WS<sub>2</sub> heterostructures for flexible and transparent electronics,” *Nature nanotechnology* **8**, 100–103 (2013).

<sup>17</sup> Humberto Terrones, Florentino López-Urías, and Mauricio Terrones, “Novel hetero-layered materials with tunable direct band gaps by sandwiching different metal disulfides and diselenides,” *Scientific reports* **3** (2013).

<sup>18</sup> Mahdi Ghorbani-Asl, Paul D Bristowe, K Koziol, Thomas Heine, and Agnieszka Kuc, “Effect of compression on the electronic, optical and transport properties of MoS<sub>2</sub>/graphene-based junctions,” *2D Materials* **3**, 025018 (2016).

<sup>19</sup> Wei Hu, Tian Wang, Ruiqi Zhang, and Jinlong Yang, “Effects of interlayer coupling and electric fields on the electronic structures of graphene and MoS<sub>2</sub> heterobilayers,” *Journal of Materials Chemistry C* **4**, 1776–1781 (2016).

<sup>20</sup> Lili Yu, Yi-Hsien Lee, Xi Ling, Elton J. G. Santos, Yong Cheol Shin, Yuxuan Lin, Madan Dubey, Eftimios Kaxiras, Jing Kong, Han Wang, and Toms Palacios, “Graphene/mos2 hybrid technology for large-scale two-dimensional electronics,” *Nano Letters* **14**, 3055–3063 (2014).

<sup>21</sup> Tribhuwan Pandey, Avinash P Nayak, Jin Liu, Samuel T Moran, Joon-Seok Kim, Lain-Jong Li, Jung-Fu Lin, Deji Akinwande, and Abhishek K Singh, “Pressure-induced charge transfer doping of monolayer graphene/MoS<sub>2</sub> heterostructure,” *Small* **12**, 4063–4069 (2016).

<sup>22</sup> Wencan Jin, Po-Chun Yeh, Nader Zaki, Daniel Chenet, Ghidewon Arefe, Yufeng Hao, Alessandro Sala, Tevfik Onur Mentes, Jerry I Dadap, Andrea Locatelli, *et al.*, “Tuning the electronic structure of monolayer graphene/MoS<sub>2</sub> van der waals heterostructures via interlayer twist,” *Physical Review B* **92**, 201409 (2015).

<sup>23</sup> Jianping Shi, Mengxi Liu, Jinxiu Wen, Xibiao Ren, Xiebo Zhou, Qingqing Ji, Donglin Ma,

Yu Zhang, Chuanhong Jin, Huanjun Chen, *et al.*, “All chemical vapor deposition synthesis and intrinsic bandgap observation of MoS<sub>2</sub>/graphene heterostructures,” *Advanced Materials* **27**, 7086–7092 (2015).

<sup>24</sup> Abbas Ebnonnasir, Badri Narayanan, Suneel Kodambaka, and Cristian V Ciobanu, “Tunable MoS<sub>2</sub> bandgap in MoS<sub>2</sub>-graphene heterostructures,” *Applied Physics Letters* **105**, 031603 (2014).

<sup>25</sup> Xingen Liu and Zhongyao Li, “Electric field and strain effect on graphene-MoS<sub>2</sub> hybrid structure: Ab initio calculations,” *The Journal of Physical Chemistry Letters* **6**, 3269–3275 (2015).

<sup>26</sup> Yu-Chuan Lin, Jun Li, Sergio C. de la Barrera, Sarah M. Eichfeld, Yifan Nie, Rafik Addou, Patrick C. Mende, Robert M. Wallace, Kyeongjae Cho, Randall M. Feenstra, and Joshua A. Robinson, “Tuning electronic transport in epitaxial graphene-based van der waals heterostructures,” *Nanoscale* **8**, 8947–8954 (2016).

<sup>27</sup> Yuan Liu, Hao Wu, Hung-Chieh Cheng, Sen Yang, Enbo Zhu, Qiyuan He, Mengning Ding, Dehui Li, Jian Guo, Nathan O. Weiss, Yu Huang, and Xiangfeng Duan, “Toward barrier free contact to molybdenum disulfide using graphene electrodes,” *Nano Letters* **15**, 3030–3034 (2015).

<sup>28</sup> Dongri Qiu and Eun Kyu Kim, “Electrically Tunable and Negative Schottky Barriers in Multi-layered Graphene/MoS<sub>2</sub> Heterostructured Transistors,” *Scientific Reports* **5**, 13743 (2015).

<sup>29</sup> Chandra Sekhar Rout, Padmashree D. Joshi, Ranjit V. Kashid, Dilip S. Joag, Mahendra A. More, Adam J. Simbeck, Morris Washington, Saroj K. Nayak, and Dattatray J. Late, “Enhanced field emission properties of doped graphene nanosheets with layered SnS<sub>2</sub>,” *Applied Physics Letters* **105**, 043109 (2014), 10.1063/1.4892001.

<sup>30</sup> K. Zhou, D. Wickramaratne, S. Ge, S. Su, A. De, and R. K. Lake, “Interlayer resistance of misoriented MoS<sub>2</sub>,” *arXiv* (2016).

<sup>31</sup> Georg Kresse and Jürgen Furthmüller, “Efficient iterative schemes for ab initio total-energy calculations using a plane-wave basis set,” *Phys. Rev. B* **54**, 11169–11186 (1996).

<sup>32</sup> Georg Kresse and Jürgen Hafner, “Ab initio molecular dynamics for liquid metals,” *Phys. Rev. B* **47**, 558–561 (1993).

<sup>33</sup> Georg Kresse and Jürgen Furthmüller, “Efficiency of ab-initio total energy calculations for metals and semiconductors using a plane-wave basis set,” *Computational Materials Science* **6**, 15–50 (1996).

<sup>34</sup> Peter E Blöchl, “Projector augmented-wave method,” *Phys. Rev. B* **50**, 17953–17979 (1994).

<sup>35</sup> John P. Perdew, J. A. Chevary, S. H. Vosko, Koblar A. Jackson, Mark R. Pederson, D. J. Singh, and Carlos Fiolhais, “Atoms, molecules, solids, and surfaces: Applications of the generalized gradient approximation for exchange and correlation,” *Phys. Rev. B* **46**, 6671–6687 (1992).

<sup>36</sup> Yue Wang and John P. Perdew, “Correlation hole of the spin-polarized electron gas, with exact small-wave-vector and high-density scaling,” *Phys. Rev. B* **44**, 13298–13307 (1991).

<sup>37</sup> G. Kresse and D. Joubert, “From ultrasoft pseudopotentials to the projector augmented-wave method,” *Phys. Rev. B* **59**, 1758–1775 (1999).

<sup>38</sup> Judith Harl, Laurids Schimka, and Georg Kresse, “Assessing the quality of the random phase approximation for lattice constants and atomization energies of solids,” *Phys. Rev. B* **81**, 115126 (2010).

<sup>39</sup> Jochen Heyd, Gustavo E. Scuseria, and Matthias Ernzerhof, “Hybrid functionals based on a screened coulomb potential,” *The Journal of Chemical Physics* **118**, 8207–8215 (2003).

<sup>40</sup> Christof Gaiser, Thorsten Zandt, Alica Krapf, Ralf Serverin, Christoph Janowitz, and Recardo Manzke, “Band-gap engineering with  $\text{HfS}_x\text{Se}_{2-x}$ ,” *Physical Review B* **69**, 075205 (2004).

<sup>41</sup> Daniel S Koda, Friedhelm Bechstedt, Marcelo Marques, and Lara K Teles, “Coincidence lattices of 2d crystals: Heterostructure predictions and applications,” *The Journal of Physical Chemistry C* **120**, 10895–10908 (2016).

<sup>42</sup> Nathaniel Gillgren, Darshana Wickramaratne, Yanmeng Shi, Tim Espiritu, Jiawei Yang, Jin Hu, Jiang Wei, Xue Liu, Zhiqiang Mao, Kenji Watanabe, Takashi Taniguchi, Marc Bockrath, Yafis Barlas, Roger K Lake, and Chun Ning Lau, “Gate tunable quantum oscillations in air-stable and high mobility few-layer phosphorene heterostructures,” *2D Materials* **2**, 011001 (2015).

<sup>43</sup> Graeme Henkelman, Andri Arnaldsson, and Hannes Jónsson, “A fast and robust algorithm for bader decomposition of charge density,” *Computational Materials Science* **36**, 354–360 (2006).

<sup>44</sup> Rajesh Kappera, Damien Voiry, Sibel Ebru Yalcin, Brittany Branch, Gautam Gupta, Aditya D Mohite, and Manish Chhowalla, “Phase-engineered low-resistance contacts for ultrathin  $\text{MoS}_2$  transistors,” *Nature materials* **13**, 1128–1134 (2014).

<sup>45</sup> J. C. Lin, S. Y. Yu, and S. E. Mohney, “Characterization of low-resistance ohmic contacts to n- and p-type InGaAs,” *Journal of Applied Physics* **114**, 044504 (2013).